Geophysical Research Letters

RESEARCH LETTER
10.1029/2022GL101622

Improved MJO Forecasts Using the Experimental Global-Nested GFDL SHiELD Model

Breanna L. Zavadoff[1], Kun Gao[2,3], Hosmay Lopez[4], Sang-Ki Lee[4], Dongmin Kim[1,4], and Lucas M. Harris[2]

[1]Cooperative Institute for Marine and Atmospheric Studies, University of Miami, Miami, FL, USA, [2]NOAA/Geophysical Fluid Dynamics Laboratory, Princeton, NJ, USA, [3]Cooperative Institute for Modeling the Earth System, Princeton University, Princeton, NJ, USA, [4]NOAA/Atlantic Oceanographic and Meteorological Laboratory, Miami, FL, USA

Abstract Sitting at the crossroads of weather and climate, the Madden-Julian Oscillation (MJO) is considered a primary source of subseasonal predictability. Despite its importance, numerical models struggle with MJO prediction as its convection moves through the complex Maritime Continent (MC) environment. Motivated by the ongoing effort to improve MJO prediction, we use the System for High-resolution prediction on Earth-to-Local Domains (SHiELD) model to run two sets of forecasts, one with and one without a nested grid over the MC. By efficiently leveraging high-resolution grid spacing, the nested grid reduces amplitude and phase errors and extends the model's predictive skill by about 10 days. These enhancements are tied to improvements in predicted zonal wind from the Indian Ocean to the Pacific, facilitated by westerly wind bias reduction in the nested grid. Results from this study suggest that minimizing circulation biases over the MC can lead to substantial advancements in skillful MJO prediction.

Plain Language Summary The Madden-Julian Oscillation, a large-scale system that moves west to east from the Indian Ocean to the Pacific Ocean over the course of 2–3 months, exerts significant influence on atmospheric circulation worldwide. Nestled somewhere between near-term weather and long-term climate, accurate prediction of the Madden-Julian Oscillation can be used to extend forecasts into the subseasonal, or 3–4 weeks range. In this study the global-scale System for High-resolution prediction on Earth-to-Local Domains model is used to run two sets of forecasts, one with and one without an advanced grid integrated into the global model over and around Indonesia. This region, known as the Maritime Continent, is a troublesome area for Madden-Julian Oscillation prediction in numerical models due to its complex environment, which makes it a prime target for the advanced grid. Integrating the advanced grid into the forecasts is shown to extend the skill of Madden-Julian Oscillation predictions by about 10 days and improve their accuracy. These enhancements are tied to a better representation of the wind field in the advanced grid area, which suggests that substantial advancements in predicting the Madden-Julian Oscillation can be made by simply minimizing circulation biases over the Maritime Continent in numerical models.

Key Points:

- Integrating a nested grid over the Maritime Continent (MC) in SHiELD extends Madden-Julian Oscillation (MJO) prediction skill by about 10 days with enhanced reliability
- Positive impacts imparted by the two-way nested grid on the MJO extend beyond the confines of the nested region
- An improved representation of the mean circulation over the MC in the nested grid contributes to substantial advancements in MJO prediction

Supporting Information:

Supporting Information may be found in the online version of this article.

Correspondence to:

B. L. Zavadoff,
bzavadoff@earth.miami.edu

Citation:

Zavadoff, B. L., Gao, K., Lopez, H., Lee, S.-K., Kim, D., & Harris, L. M. (2023). Improved MJO forecasts using the experimental global-nested GFDL SHiELD model. *Geophysical Research Letters*, *50*, e2022GL101622. https://doi.org/10.1029/2022GL101622

Received 6 OCT 2022
Accepted 12 JAN 2023

1. Introduction

The Madden-Julian Oscillation (MJO; Madden & Julian, 1971; Madden & Julian, 1972) is a large-scale convection-circulation couplet that propagates from the Indian Ocean to the western Pacific at approximately 5 m s^{-1} (Zhang, 2005). With a period of 40–50 days the MJO is widely known as the dominant mode of tropical variability on subseasonal timescales, significantly influencing the Asian (Lau & Chan, 1986; Zhang, 2005), Australian (Wheeler et al., 2009) and West African (Lavender & Matthews, 2009) monsoons as well as tropical cyclone development worldwide (Alaka & Maloney, 2012; Camargo et al., 2009; Klotzbach, 2010; Liebmann et al., 1994; Maloney & Hartmann, 2000a, 2000b; Ventrice et al., 2011). The MJO has also been found to modulate the El Niño/Southern Oscillation, such that enhanced (reduced) MJO activity in the western Pacific generates westerly (easterly) wind anomalies that extend (contract) the eastern edge of the Pacific warm pool and promote El Niño (La Niña) development (Hendon et al., 2007; Zhang, 2013). Though the physical mechanisms of the MJO are confined to the lower latitudes, its effects on weather and climate extend well beyond the tropics. Rossby wave excitement via MJO-related latent heat release has been shown to modify extratropical flow patterns from the North Pacific to the North Atlantic (Higgins & Mo, 1997; Moore et al., 2010; Mori & Watanabe, 2008; Seo & Lee, 2017; Tseng et al., 2019), impacting atmospheric blocking (Henderson et al., 2016; Moore et al., 2010; Stan et al., 2017) and climate modes (Cassou, 2008; Mori & Watanabe, 2008; Zhang, 2013) throughout these regions.

Given its substantial impact on both weather and climate throughout the world, the MJO is considered one of the primary sources of global subseasonal predictability (H. Kim et al., 2018; Vitart et al., 2017; Zhang, 2013). In recent years numerical models have improved their MJO prediction skill due to enhancements in observation collection, data assimilation, and the models themselves (Ahn et al., 2017; H. Kim et al., 2018). For instance, skillful prediction of the MJO in the National Center for Environmental Prediction (NCEP) Climate Forecast System improved from 10 to 15 days in version 1 to approximately 3 weeks in version 2 (Lim et al., 2018; Wang et al., 2014). Even more dramatic advancements have been made in the European Centre for Medium-Range Weather Forecasts model, which has progressed from 22 days of skillful prediction in 2002 (Vitart, 2014) to 33–36 days nearly 2 decades later (Lim et al., 2018; H. Kim et al., 2019).

MJO prediction skill has been shown to be sensitive to a number of factors including initial amplitude, such that forecasts initialized with a strong MJO generally have higher predictive skill than those initialized with a weak MJO (H.-M. Kim et al., 2014; Lim et al., 2018; Lin et al., 2008; Rashid et al., 2011; Wang et al., 2014). Skillful MJO prediction is also closely tied to a model's ability to realistically simulate its eastward propagation (Gonzalez & Jiang, 2017; Lim et al., 2018; H. Kim et al., 2018). Known to be a chronic problem in numerical models, MJO propagation suffers substantially as the system moves through the Maritime Continent (MC; H.-M. Kim et al., 2014; H. Kim et al., 2019; Wang et al., 2014). The MC is a particularly difficult region for MJO prediction and serves as an MJO "prediction barrier" (Abhik et al., 2022; H.-M. Kim et al., 2016) due to its complex orography, multi-scale ocean-atmospheric interactions, and strong diurnal convection (H. Kim et al., 2018) that serve to weaken and/or dissolve convection.

As part of the continued effort to improve MJO prediction, in this study a series of forecasts are produced using the new GFDL System for High-resolution prediction on Earth-to-Local Domains (SHiELD) model (Harris et al., 2020). SHiELD has exhibited better large-scale prediction skill, precipitation prediction skill, and diurnal cycle representation compared to existing climate models, all important factors for MJO prediction. A concurrent set of forecasts is also developed utilizing a nested grid over the MC in an attempt to ameliorate the ramifications of the MC barrier effect.

2. Data and Methods

2.1. Observational Data

Daily averaged zonal winds at 850 hPa (u850) and 200 hPa (u200) from the NCEP/National Center for Atmospheric Research (NCAR) reanalysis data set version 1 (Kalnay et al., 1996) are used in conjunction with daily interpolated outgoing longwave radiation (OLR) from the National Oceanographic and Atmospheric Administration (NOAA; Liebmann & Smith, 1996) to compute the combined empirical orthogonal functions (EOFs; Figure S1 in Supporting Information S1) used to derive the real-time multivariate MJO index 1 (RMM1) and 2 (RMM2) for MJO identification (Text S1 in Supporting Information S1; Wheeler & Hendon, 2004) in the model forecasts and time-matched observations for verification. Zonal wind data from the NCEP/NCAR reanalysis data set are also used to compare the models' large-scale wind fields to that of observations to identify any potential circulation biases present within each model configuration. Daily averaged precipitation rate estimates from the Global Precipitation Climatology Project (GPCP; Huffman et al., 2001) are used to compare latitudinally averaged daily rainfall totals in observations to those produced by the model forecasts. Most of the previously described data sets have a horizontal resolution of 2.5° × 2.5°, which is much coarser than SHiELD's post-processed 1° × 1° grid. Under circumstances when the observational and model fields have different resolutions and are being compared, the observed data is linearly interpolated to the higher resolution SHiELD grid to allow for a more direct comparison between the data sets.

2.2. Model Specifications

The model used in this study is the GFDL SHiELD (Harris et al., 2020), which uses the nonhydrostatic GFDL Finite-Volume Cubed-Sphere Dynamical Core (Harris et al., 2021; Putman & Lin, 2007) and a suite of physical parameterizations originating from the operational Global Forecast System (GFS). MJO forecasts based on two grid configurations are compared in this study. In the control configuration (SHiELD control), a global uniform 16 km resolution grid is used. In the two-way nested configuration (SHiELD nested), a large nest with a nominal resolution of 4 km covering the Bay of Bengal, MC and part of the western Pacific (79°E−164°E and 14°S–14°N;

Figure S2 in Supporting Information S1) is integrated into the global grid. Both the global and nested grids use 63 vertical levels as in Harris et al. (2020).

For the present study, we use the GFDL single-moment five-category microphysics scheme (Zhou et al., 2019), the Yonsei University boundary layer scheme (Hong et al., 2006), the scale-aware deep and shallow convection parameterization (Han et al., 2017), and the Rapid Radiative Transfer Model for General Circulation Models (Iacono et al., 2008) radiation scheme. The deep convection parameterization is enabled in the global domain but disabled in the nested domain. The model also uses a simple mixed layer ocean (MLO) model (Pollard et al., 1973) as a crude way to represent the feedback from an interactive ocean. Harris et al. (2020) demonstrated that even using the simple MLO model can substatinally improve the MJO prediction compared to the case when fixed sea surface temperature (SST) is used. As in Harris et al. (2020), the SST during the forecast is nudged toward the observed SST climatology plus a fixed initial SST anomaly with a relaxation time scale of 15 days.

Each of the grid configurations described above are used to produce a set of 40-day forecasts. Running on 3,072 Intel Xeon CPU cores, one two-way nested 40-day forecast can be generated in only 9.6 hr, making it 10x less expensive than the approximately 28 hr and 13,824 cores needed for a single globally-uniform high-resolution run. This highlights the efficiency of the two-way nested configuration to produce forecasts that leverage the embedded 4 km grid spacing. Forecasts are initialized with the operational GFS analysis on a daily basis, that is, one day apart from each other, from 13 October 2011 to 30 November 2011 and 19 February 2012 to 4 March 2012, for a total of 64 forecasts per configuration (128 in total). These periods were chosen for analysis as they coincide with the Cooperative Indian Ocean Experiment on Intraseasonal Variability/Dynamics of the MJO (CINDY/DYNAMO) field campaign during which frequent and strong MJO activity was recorded, as shown in Figure S3 in Supporting Information S1.

3. Results

3.1. Deterministic Skill Assessment

To assess how well the models' predicted MJO strength and location compare to observations, squared amplitude and phase errors are calculated (Text S2 in Supporting Information S1) as a function of lead time for all forecasts (Figures 1a and 1b). While both models exhibit a tendency to produce a stronger MJO than observed (Figure 1a, Figure S4 in Supporting Information S1), the overall amplitude error is less severe at all lead times in the nested forecasts. This may be attributed in part to refinements in the representation of the large-scale scale zonal winds. As shown in Li et al. (2019), models whose zonal winds most closely matched that of observations from the Indian Ocean to the western Pacific exhibited better overall MJO predictability as well as reduced errors in amplitude and phase. With the inclusion of the nested grid, westerly wind biases are reduced over portions of the MC in the u200 (Figure S5 in Supporting Information S1) and u850 (Figure S6 in Supporting Information S1) fields. A marked area of improvement is also apparent over the central Indian Ocean, where a large westerly wind bias in the control forecasts is largely diminished in the nested forecasts. This shows that the positive impacts imparted by the two-way nested grid extend beyond the confines of the nested region.

When it comes to predicted phase, both models produce an MJO that at times propagates slower and at other times propagates faster than the observed MJO (Figure S4 in Supporting Information S1). Each models' phase prediction performance relative to observations can be more clearly explained through squared phase error calculations. As shown in Figure 1b, the nested forecasts produce an MJO with a predicted phase closer to that in observations than the control forecasts at all lead times. These results suggest that forecasts generated with the nested grid produce a more realistic MJO with respect to both predicted amplitude and phase.

MJO prediction skill is evaluated by calculating bivariate anomaly correlation coefficient (ACC; Figures 1c, 1d and 1e; Text S2 in Supporting Information S1) and bivariate root mean square error (RMSE; Figures 1f, 1g, 1h; Text S2 in Supporting Information S1) for all forecasts in each model. Both model configurations display skillful MJO prediction throughout the first few weeks of the forecast and follow a similar rate of decline in ACC until day 22. After this point the skill of the control forecasts sharply decreases, dropping below 0.5 by day 26. The skill of the nested forecasts also continues to decline after day 22, but at a much slower rate such that it extends another 10 days beyond that of the control forecasts, finally dropping below 0.5 after 35 days. These results indicate that the inclusion of the nested grid improves MJO prediction the most at longer lead times. This is due to the improved model physics found within the nested grid that foster the simulation of a more realistic MJO than those found in the control forecasts once the influence of the initial conditions is lost.

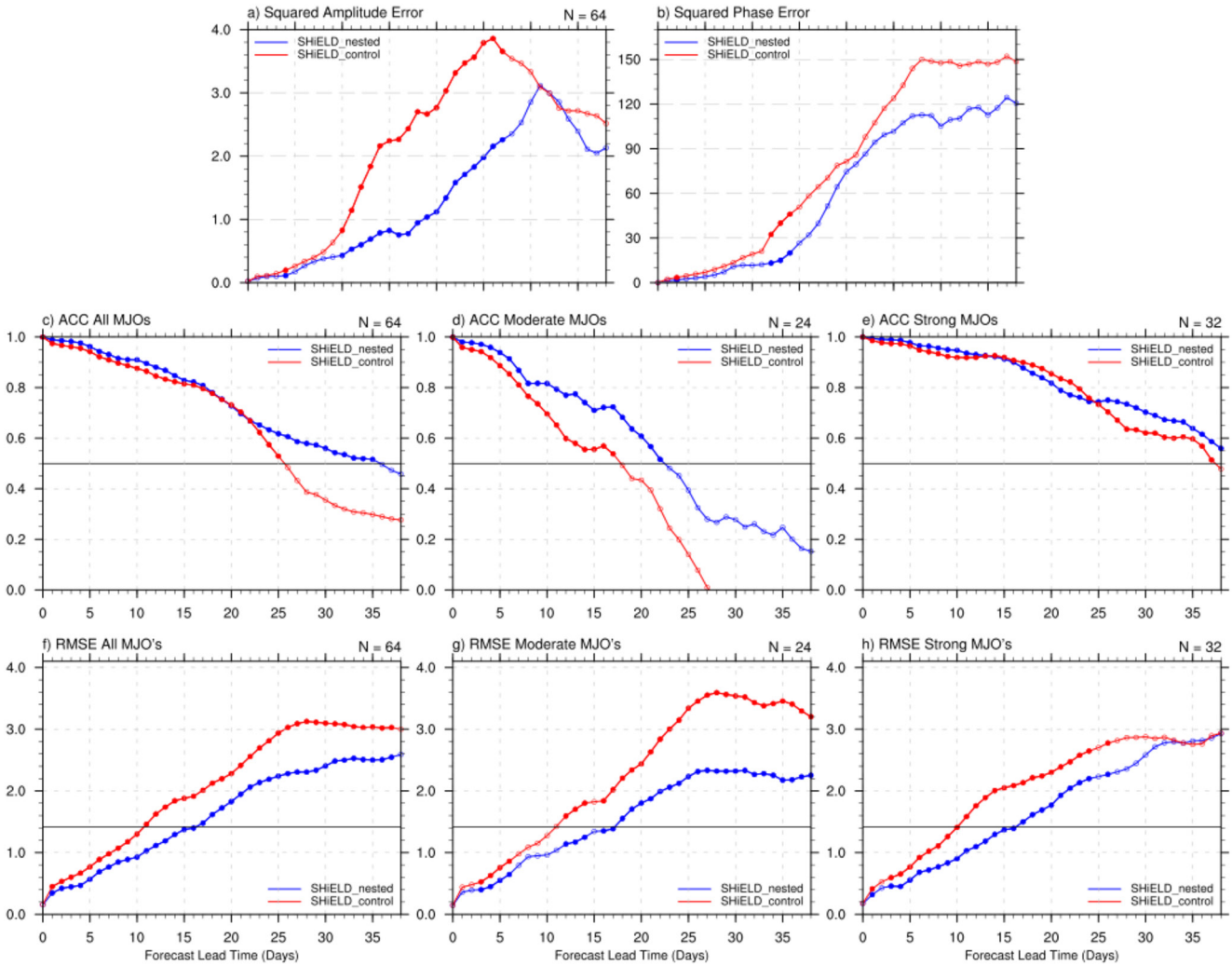

Figure 1. (a) Squared amplitude and (b) phase (degrees) errors as a function of lead time for all 64 forecasts. Blue and red curves correspond to SHiELD nested forecasts and SHiELD control forecasts, respectively. ACC (c, d, e) and RMSE (f, g, h) curves as a function of lead time for (c, f) all 64 forecasts, (d, g) forecasts initialized with a moderate MJO, and (e, h) forecasts initialized with a strong MJO. Horizontal lines in (c, d, e) and (f, g, h) correspond to skillful prediction thresholds of 0.5 and $\sqrt{2}$, respectively. The sample size of each subgroup is provided in the top right corner. Filled circles in (a, b, f, g, h) correspond to lead times where the difference between the nested and control forecasts are statistically significant at the 95% confidence level according to a Student's *t* test. In (c–e), filled circles represent lead times where the ACC is ≥ 0.5.

Enhanced MJO prediction skill in the nested forecasts is also evident through RMSE calculations. Figure 1f shows that, for all lead times the nested forecasts exhibit a lower RMSE than the control forecasts. Furthermore, the nested forecasts' RMSE remains below the $\sqrt{2}$ skillful prediction threshold for nearly an entire week longer than the control forecasts. As shown throughout Figure 1, inclusion of the nested grid facilitates the most sizable improvements in ACC and RMSE at longer lead times. This is likely due to the notable squared phase error reductions exhibited later in the nested forecasts because even though MJO prediction skill is dependent on both squared amplitude and squared phase error, it is more sensitive to the latter, especially at longer lead times (Lim et al., 2018).

Previous works have established that a model's MJO predictive skill is sensitive to the initial amplitude of the MJO in the forecast. To test if this is also true in SHiELD, forecasts are separated into two groups based on their initial amplitude. Though forecasts are traditionally separated into strong and weak groups based on a threshold amplitude of 1 (H. Kim et al., 2018; Lin et al., 2008; Neena et al., 2014), nearly all of the forecasts in our data set are initialized with an MJO amplitude ≥1 due to the very strong and active MJOs that occurred during the analysis period (Figure S3 in Supporting Information S1). Therefore, forecasts that are initialized with an MJO

amplitude ≥2 are sorted into the strong group, while those initialized with an MJO amplitude ≥1 but <2 are sorted into the moderate group. Forecasts initialized with an MJO in the neutral/weak phase are hereafter excluded from the analysis because the purpose of the nested grid is to determine how its inclusion helps to improve the model's performance in predicting an active-convective MJO (amplitude ≥1).

Consistent with previous studies (Lim et al., 2018; Rashid et al., 2011; Wang et al., 2014; Wu et al., 2016), forecasts initialized with a strong MJO have skillful MJO prediction through longer lead times than those initialized with a moderate strength MJO. Predictive skill in the control forecasts more than doubled from 17 days for moderate MJOs (Figures 1d) to 37 days for strong MJOs (Figure 1e). A similar jump was observed in the nested forecasts in which predictability was extended from 22 days to a point beyond the forecast period for initially moderate and strong MJOs, respectively. With respect to the RMSE curves, predictive skill for strong MJO forecasts remain relatively unchanged (Figure 1h). Conversely, the RMSE curves for forecasts initialized with moderate MJOs indicate a predictive skill increase by about 1 day for both configurations (Figure 1g). Additionally, despite both configurations gaining a day of predictive skill, the RMSE curve of the moderate MJO nested forecasts remains significantly lower than that of the control forecasts at longer lead times. These findings are insensitive to the amplitude chosen to delineate between strong and moderate MJOs.

The results presented in Figure 1 reveal that integrating the nested grid into SHiELD improves the model's deterministic MJO prediction skill across the board. Notably, the differences between the nested and control configurations are statistically significant at most lead times for squared amplitude error and RMSE. This suggests that the two models have very distinct variances from one another, hence why the nested forecasts reproduce observations much better and possess greater MJO prediction skill (Figures 1c–1e) than the control forecasts. These results also indicate that the nested grid provides the most benefit to forecasts with a moderate strength MJO. These enhancements are on full display in composite Hovmöller diagrams of daily precipitation rate for forecasts initialized with an MJO in phases 2 and 3 (Figure S7 in Supporting Information S1). Inclusion of the nested grid improves the forecast via the breakdown of the original MJO signal over the MC as well as the capture of an emerging MJO signal in the Indian Ocean late in the forecast period, features virtually absent from the control forecasts.

3.2. Probabilistic Skill Assessment

Since the sample size of the data is limited, time-lagged ensembles of u200, u850, and OLR intraseasonal anomalies are built that target forecasts at lead times of 21–30 days from each daily initial condition (i.e., 2 pentads in weeks 4 and 5 lead), so that we have 10 ensemble members targeting 1 day (i.e., observation). For instance, if we set our target date as December 1 we can construct a 10 member forecast ensemble by extracting data for December 1 from all forecasts initialized between November 1 (30 days lead time) and November 10 (21 days lead time). The choice of lead time was motivated by the analysis presented in Figure 1, which shows that the greatest improvements in RMSE and ACC due to the two-way nested grid emerge around this time. Recall that there are 64 forecasts in this data set for each model. However, given the size of the time-lag ensemble and gaps between our simulation periods in the middle of the data set, this set up only provides 28 target days (i.e., days for which at least 10 ensembles provide forecasts). Since probabilistic analysis is sensitive to degrees of freedom, we aggregate all longitude points and evaluate all forecasts at each longitude grid point along the equator and time (28×360). Several probabilistic skill metrics were chosen for use in this analysis (Text S3 in Supporting Information S1) and are presented in Figure 2: the reliability diagram (Atger, 1999; Murphy & Winkler, 1977), Brier skill score (BSS; Kharin & Zwiers, 2003; Toth et al., 2003), and relative operating characteristics (ROC; Swets, 1973; Mason & Graham, 1999).

Overall, both our reliability and ROC diagrams indicate that the nested forecasts are more reliable in predicting u200, u850, and OLR for all probabilistic metrics. The reliability diagrams (Figures 2a, 2c and 2e) show that the two-way nested grid improves the calibration of the model by bringing more forecast probabilities (e.g., dots) closer to the diagonal line within the green shaded area than in the control configuration, which indicates a better representation of forecast probabilities versus observed frequencies and subsequently shifts the reliability calculation closer to zero. Additionally, the frequency resolution (not to be confused with grid resolution) of the forecasts increases in the nested forecasts, depicting better representation of the observed frequency. This is represented through both a higher number for the resolution calculation and a larger vertical range of observed frequencies far away from the "no resolution" line. While both models predict events with probabilities different

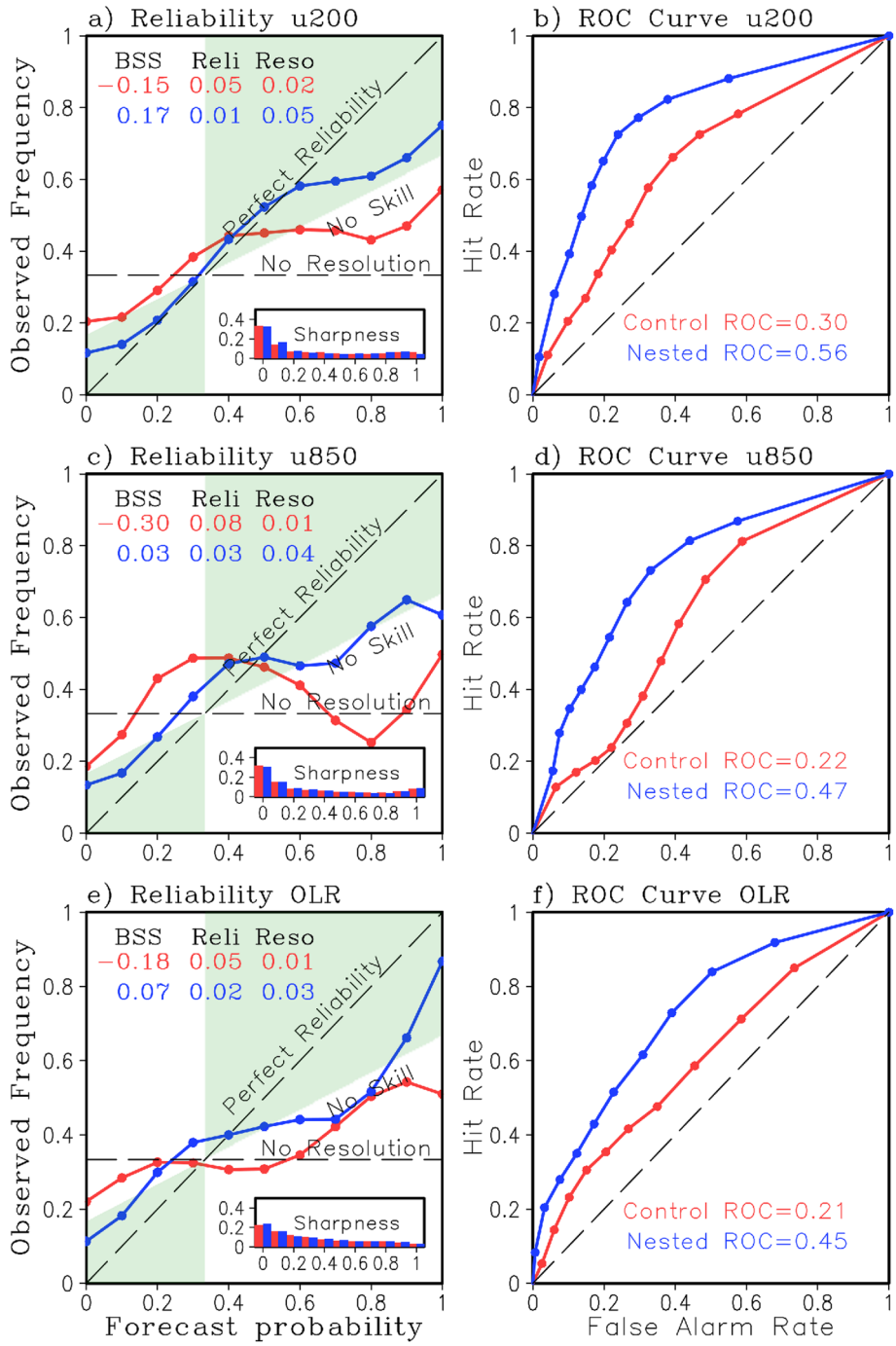

Figure 2. Probabilistic forecast skill assessment for SHiELD control (red) and nested (blue) forecasts against observations at 21–30 days lead times (weeks 4 and 5). Reliability diagrams (left) showing forecast probability (abscissa) versus observed frequency (ordinate) for (a) u200, (c) u850, and (e) OLR, conditioned on each of the $I = 11$ possible probability forecasts. Points within the green shaded regions contribute positively to forecast skill. The relative frequencies of each forecast are shown within the inserted panel labeled "sharpness." Numerical entries denoted by BSS, Reli, and Reso correspond to the Brier skill score, reliability, and resolution indices, respectively. Relative operating characteristics (ROC) curves (right) comparing false alarm rates (abscissa) to hit rates (ordinate) for (b) u200, (d) u850, and (f) OLR, conditioned on each of the $I = 11$ possible probability forecasts. Numerical values denote the ROC scores (i.e., area between the curves and the diagonal), which range from −1 to 1. A score of zero denotes no skill.

from the observed event climatology (i.e., sharpness), the nested forecasts do so with increased reliability and resolution, thus reducing the chance of issuing false alarms and missed forecasts, which culminates in an overall higher BSS. For the ROC diagrams (Figures 2b, 2d and 2f), the nested forecast line is consistently closer to the top-left than the control forecast line, which indicates that the nested forecasts have a higher number of hit rates and lower number of the false alarm rates (i.e., higher skill) than the control forecasts. This is further supported by the ROC score index shown in the bottom-center of each panel, in which a higher score indicates higher probabilistic skill.

Of the three variables analyzed here u200 is by far the most predictable, exhibiting the best BSS, resolution, reliability, and ROC scores (Figures 2a and 2b). In addition to the high marks, all forecast probabilities for the nested forecasts lie within the green region on the u200 reliability diagram (Figure 2a). Some of these forecast probabilities even lie along the "perfect reliability" line, something not achieved by any other variable/configuration combination. When it comes to u850, some of the highest forecast probabilities in the control configuration are extremely overconfident with respect to the observed frequencies and even exhibit less skill than climatology by dipping below the "no resolution" line (Figure 2c). These deficiencies are notably improved in the nested forecasts, with the highest forecast probabilities found much closer to the diagonal line and, in some cases, within the green area. Furthermore, an appreciable segment of the control forecast u850 ROC curve is found to be very close to the diagonal or "no skill" line (Figure 2d). This indicates that the control forecasts have incredibly low probabilistic skill when it comes to low forecast probabilities, a deficiency that is absent in the nested forecasts. Similarly to u200 and u850, the nested grid serves to improve the reliability and skill of OLR prediction over the control configuration (Figures 2e and 2f). These results serve to add robustness to our deterministic skill assessment and support the conclusion that forecasts run with the two-way nested SHiELD configuration outperform and have a higher skill than those forecasts run with the control configuration.

3.3. Sources of Predictability

Inclusion of the nested grid also improves MJO prediction via a more realistic representation of MJO propagation through the MC and beyond (Figures 3a–3c, 3e–3g). Strong u200 westerlies present over the western MC in the first 2 weeks of the control forecasts are diminished and contracted eastward in the nested forecasts (Figures 3b and 3c), enabling the observed longitudinal "jump" of upper level easterlies to occur in the nested MJO while remaining absent from the control MJO. An overall reduction of the u850 westerly and, to a lesser degree, easterly wind biases in the nested configuration (Figure 3f), produce a more realistically structured MJO that begins to weaken once it reaches the western Pacific. Conversely, in the control configuration (Figure 3g) an overly amplified system is forecast, which results in an MJO signal that remains generally intact upon reaching the western Pacific. When it comes to OLR, at shorter lead times the nested forecasts exhibit convection is significantly weakened over the eastern Indian Ocean (Figure 3k) compared to observations and the control forecasts (Figures 3i and 3j). However, over the MC the nested grid serves to strengthen a region of convection that is generally absent in the control forecasts. These convection differences between the two configurations can be clearly seen in Figure 3l. At longer lead times, both the control and nested forecasts produce an MJO with a similar eastward propagation and an OLR anomaly signal that is greatly diminished compared to observations. Though only in isolated areas, MJO-related field differences between model configurations (Figures 3d, 3h, 3l) are found to be statistically significant throughout the 40-day forecast period both in and outside of the nested grid region, reinforcing the idea that the nested grid has a constant effect on the MJO that reaches beyond its borders. Improvements in MJO simulated strength and structure due to the nested grid can also be seen in Figure S7 in Supporting Information S1. Similarly to previous studies (Holloway et al., 2013; Jia et al., 2008; Savarin & Chen, 2022), enhanced model resolved convection in the higher-resolution nested grid allows for a more realistic representation of precipitation rate and distribution for both strong and moderate strength MJOs compared to the parameterized convection used in the coarser global grid.

To elucidate which of the MJO related variables contributes to predictability improvements in the nested configuration, ACC for u200, u850, and OLR were calculated for all forecasts initialized with an active MJO (Figures S8, S9 in Supporting Information S1). Similarly to (Li et al., 2019), enhanced predictability in the nested forecasts is related to higher correlations between predicted u200 and observed u200 over the Indian Ocean at long lead times as well as the western half of the MC at shorter lead times. These two areas correspond to the regions where westerly wind biases present in the control forecasts are reduced in the nested forecasts (Figure

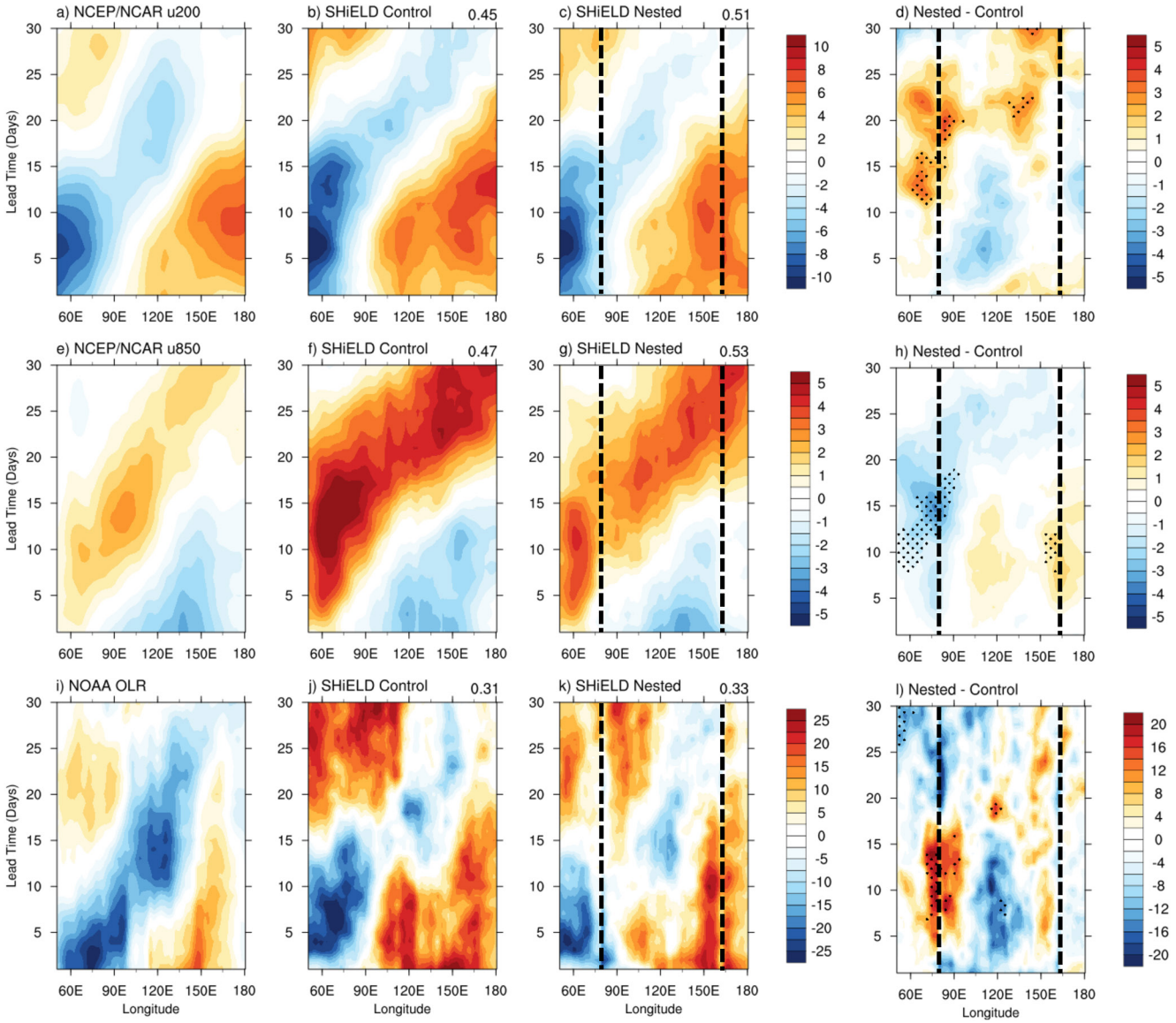

Figure 3. Composite Hovmöller diagrams of latitudinally averaged (15°S–15°N) daily intraseasonal anomalies (shaded according to colorbar) of u200 (m s^{-1}; top), u850 (m s^{-1}; middle), and OLR (W m^{-2}; bottom) as a function of lead time and longitude for (a, e, i) observations time matched to the 35 (b, f, j) SHiELD control and (c, g, k) nested forecasts initialized with an MJO in Phase 2 or 3. Differences between the nested and control forecasts for each variable are shown in (d, h, l) and stippling indicates regions where these differences are statistically significant at the 95% confidence level according to a Student's *t* test. Black dashed lines in (c, g, k) and (d, h, j) denote the longitudinal boundaries of the two-way nested grid. Pearson correlation coefficients for each modeled variable compared to observations are presented in the top right corner.

S5 in Supporting Information S1). As in Li et al. (2019), of the three variables OLR contributes the least to MJO predictability (Figure S9 in Supporting Information S1), however, inclusion of the nested grid serves to enhance OLR prediction over the western MC at shorter lead times and the eastern Indian Ocean at lead times out to nearly 3 weeks. Increased correlations in u850 from the MC to the central Pacific at virtually all lead times (Figure S8 in Supporting Information S1) provide the foundation for extended MJO predictability in the nested forecasts, likely due to the fact that surface westerly winds associated with the MJO affect air-sea fluxes that feed back onto and are critical to the maintenance and eastward propagation of the MJO itself (DeMott et al., 2015; Savarin & Chen, 2022). As such, a more realistic representation of the near-surface winds is key to improving MJO prediction (Li et al., 2019; Nasuno, 2013), something that is achieved in the nested forecasts via amelioration of the u850 westerly wind biases from the MC to the central Pacific (Figure S6 in Supporting Information S1).

4. Summary

Improving MJO predictability in numerical models continues to be a challenging but important task for the advancement of subseasonal weather prediction worldwide. In this study, forecasts are run during the CINDY/DYNAMO period using two configurations of the GFDL SHiELD model. The first configuration corresponds to the control setup, while the second configuration includes a two-way nested grid over the MC that improves the model's performance in predicting the MJO by efficiently leveraging high resolution grid spacing. Incorporating the nested grid into SHiELD improves the model's performance with regard to predictions of MJO amplitude and phase and serves to extend skillful prediction of the MJO in SHiELD by 10 days as well as reduce the predicted RMSE. As in previous studies, forecasts initialized with a strong MJO exhibited greater predictive skill, however, forecasts initialized with a moderate strength MJO demonstrated considerable improvement in skillful prediction with the addition of the nested grid. Using time-lagged ensembles and probabilistic analyses, we were able to further demonstrate how forecasts using the two-way nested grid outperform those using the control configuration through enhancements in both reliability and skill.

Predictability improvements in the nested configuration were found to be tied to a more realistic representation of MJO propagation and increased correlations between the predicted and observed zonal winds. These higher correlations corresponded to regions with a more accurate representation of the zonal wind field due to westerly wind bias reduction in the nested forecasts from the Indian Ocean to the central Pacific. Results from this study suggest that targeting the minimization of circulation biases over the MC can lead to substantial advancements in skillful MJO prediction. This is because reducing the mean zonal wind biases could lead to subsequent improvement in the representation of the anomalous MJO circulation, which is integral for the proper simulation of both moisture advection and the eastward propagation of MJO convection (Jiang, 2017). Though encouraging, the robustness of the improvements in skillful MJO prediction exhibited here due to the inclusion of the two-way nested grid are still unknown due to the limited sample size of the data. A much larger, multi-season sample of SHiELD data would be needed to fully quantify the extent of these advancements. Data limitations also prevented the performance of any phase-based analysis in this study. Therefore, evaluating the predictive skill of forecasts initialized with an MJO over the Indian Ocean versus the MC and their subsequent downstream teleconnection development in SHiELD control and nested configurations are topics we would like to pursue in the future.

Data Availability Statement

Interpolated outgoing longwave radiation and zonal wind data from the NCEP/NCAR reanalysis data set, used for empirical orthogonal function analysis and MJO verification, is provided by the NOAA/PSL and publicly available from their website at: https://psl.noaa.gov/data/gridded/index.html. Precipitation rate estimate data from the Global Precipitation Climatology Project, used to develop composites of daily precipitation rate, is provided by the NOAA/National Centers for Environmental Information and publicly available from their website at: https://www.ncei.noaa.gov/products/climate-data-records/precipitation-gpcp-daily. All SHiELD output data utilized in this study can be accessed at: https://doi.org/10.5281/zenodo.7154177. Version 6.2.2 of the NCAR Command Language, used for data analysis and visualization, is preserved at: http://dx.doi.org/10.5065/D6WD3XH5 and available publicly for download at: https://www.earthsystemgrid.org/dataset/ncl.html.

Acknowledgments
This research was carried out in part under the auspices of the Cooperative Institute for Marine and Atmospheric Studies (CIMAS), a Cooperative Institute of the University of Miami and the National Oceanic and Atmospheric Administration, cooperative agreement #NA20OAR4320472. Support for this research was also provided by the Cooperative Institute for Modeling the Earth System (CIMES) under grant number #NA18OAR4320123. The authors would also like to thank Baoqiang Xiang, Emily Becker, and the two anonymous reviewers for their thoughtful suggestions and comments that greatly helped improve the quality of the manuscript. The statements, findings, conclusions, and recommendations are those of the author(s) and do not necessarily reflect the views of the National Oceanic and Atmospheric Administration, or the U.S. Department of Commerce.

References

Abhik, S., Hendon, H. H., & Zhang, C. (2022). The Indo-Pacific Maritime Continent barrier effect on MJO prediction. *Journal of Climate*, 1–29.

Ahn, M.-S., Kim, D., Sperber, K. R., Kang, I.-S., Maloney, E., Waliser, D., & Hendon, H. (2017). MJO simulation in CMIP5 climate models: MJO skill metrics and process-oriented diagnosis. *Climate Dynamics*, *49*(11), 4023–4045. https://doi.org/10.1007/s00382-017-3558-4

Alaka, G. J., & Maloney, E. D. (2012). The influence of the MJO on upstream precursors to African easterly waves. *Journal of Climate*, *25*(9), 3219–3236. https://doi.org/10.1175/jcli-d-11-00232.1

Atger, F. (1999). The skill of ensemble prediction systems. *Monthly Weather Review*, *127*(9), 1941–1953. https://doi.org/10.1175/1520-0493(1999)127<1941:tsoeps>2.0.co;2

Camargo, S. J., Wheeler, M. C., & Sobel, A. H. (2009). Diagnosis of the MJO modulation of tropical cyclogenesis using an empirical index. *Journal of the Atmospheric Sciences*, *66*(10), 3061–3074. https://doi.org/10.1175/2009jas3101.1

Cassou, C. (2008). Intraseasonal interaction between the Madden–Julian oscillation and the North Atlantic Oscillation. *Nature*, *455*(7212), 523–527. https://doi.org/10.1038/nature07286

DeMott, C. A., Klingaman, N. P., & Woolnough, S. J. (2015). Atmosphere-ocean coupled processes in the Madden-Julian oscillation. *Review of Geophysics*, *53*(4), 1099–1154. https://doi.org/10.1002/2014rg000478

Gonzalez, A. O., & Jiang, X. (2017). Winter mean lower tropospheric moisture over the Maritime Continent as a climate model diagnostic metric for the propagation of the Madden-Julian oscillation. *Geophysical Research Letters*, *44*(5), 2588–2596. https://doi.org/10.1002/2016gl072430

Han, J., Wang, W., Kwon, Y. C., Hong, S.-Y., Tallapragada, V., & Yang, F. (2017). Updates in the NCEP GFS cumulus convection schemes with scale and aerosol awareness. *Weather and Forecasting*, *32*(5), 2005–2017. https://doi.org/10.1175/waf-d-17-0046.1

Harris, L., Chen, X., Putman, W., Zhou, L., & Cheng, J.-H. (2021). *A scientific description of the GFDL finite-volume cubed-sphere dynamical core*. NOAA Technical Memorandum OAR GFDL.

Harris, L., Zhou, L., Lin, S.-J., Chen, J.-H., Chen, X., Gao, K., et al. (2020). GFDL SHiELD: A unified system for weather-to-seasonal prediction. *Journal of Advances in Modeling Earth Systems*, *12*(10), e2020MS002223. https://doi.org/10.1029/2020ms002223

Henderson, S. A., Maloney, E. D., & Barnes, E. A. (2016). The influence of the Madden–Julian oscillation on Northern Hemisphere winter blocking. *Journal of Climate*, *29*(12), 4597–4616. https://doi.org/10.1175/jcli-d-15-0502.1

Hendon, H. H., Wheeler, M. C., & Zhang, C. (2007). Seasonal dependence of the mjo–enso relationship. *Journal of Climate*, *20*(3), 531–543. https://doi.org/10.1175/jcli4003.1

Higgins, R. W., & Mo, K. C. (1997). Persistent North Pacific circulation anomalies and the tropical intraseasonal oscillation. *Journal of Climate*, *10*(2), 223–244. https://doi.org/10.1175/1520-0442(1997)010<0223:pnpcaa>2.0.co;2

Holloway, C. E., Woolnough, S. J., & Lister, G. M. (2013). The effects of explicit versus parameterized convection on the MJO in a large-domain high-resolution tropical case study. Part I: Characterization of large-scale organization and propagation. *Journal of the Atmospheric Sciences*, *70*(5), 1342–1369. https://doi.org/10.1175/jas-d-12-0227.1

Hong, S.-Y., Noh, Y., & Dudhia, J. (2006). A new vertical diffusion package with an explicit treatment of entrainment processes. *Monthly Weather Review*, *134*(9), 2318–2341. https://doi.org/10.1175/mwr3199.1

Huffman, G. J., Adler, R. F., Morrissey, M. M., Bolvin, D. T., Curtis, S., Joyce, R., et al. (2001). Global precipitation at one-degree daily resolution from multisatellite observations. *Journal of Hydrometeorology*, *2*(1), 36–50. https://doi.org/10.1175/1525-7541(2001)002<0036:gpaodd>2.0.co;2

Iacono, M. J., Delamere, J. S., Mlawer, E. J., Shephard, M. W., Clough, S. A., & Collins, W. D. (2008). Radiative forcing by long-lived greenhouse gases: Calculations with the AER radiative transfer models. *Journal of Geophysical Research*, *113*(D13), D13103. https://doi.org/10.1029/2008jd009944

Jia, X., Li, C., Ling, J., & Zhang, C. (2008). Impacts of a GCM's resolution on MJO simulation. *Advances in Atmospheric Sciences*, *25*(1), 139–156. https://doi.org/10.1007/s00376-008-0139-9

Jiang, X. (2017). Key processes for the eastward propagation of the Madden-Julian Oscillation based on multimodel simulations. *Journal of Geophysical Research: Atmospheres*, *122*(2), 755–770. https://doi.org/10.1002/2016jd025955

Kalnay, E., Kanamitsu, M., Kistler, R., Collins, W., Deaven, D., Gandin, L., et al. (1996). The NCEP/NCAR 40-year reanalysis project [Dataset]. Bulletin of the American Meteorological Society, *77*(3), 437–472. https://doi.org/10.1175/1520-0477(1996)077<0437:TNYRP>2.0.CO;2

Kharin, V. V., & Zwiers, F. W. (2003). Improved seasonal probability forecasts. *Journal of Climat*e, *16*(11), 1684–1701. https://doi.org/10.1175/1520-0442(2003)016<1684:ispf>2.0.co;2

Kim, H., Janiga, M. A., & Pegion, K. (2019). MJO propagation processes and mean biases in the SubX and S2S reforecasts. *Journal of Geophysical Research: Atmospheres*, *124*(16), 9314–9331. https://doi.org/10.1029/2019jd031139

Kim, H., Vitart, F., & Waliser, D. E. (2018). Prediction of the Madden–Julian oscillation: A review. *Journal of Climate*, *31*(23), 9425–9443. https://doi.org/10.1175/jcli-d-18-0210.1

Kim, H.-M., Kim, D., Vitart, F., Toma, V. E., Kug, J.-S., & Webster, P. J. (2016). MJO propagation across the Maritime Continent in the ECMWF ensemble prediction system. *Journal of Climate*, *29*(11), 3973–3988. https://doi.org/10.1175/jcli-d-15-0862.1

Kim, H.-M., Webster, P. J., Toma, V. E., & Kim, D. (2014). Predictability and prediction skill of the MJO in two operational forecasting systems. *Journal of Climate*, *27*(14), 5364–5378. https://doi.org/10.1175/jcli-d-13-00480.1

Klotzbach, P. J. (2010). On the Madden–Julian oscillation–Atlantic hurricane relationship. *Journal of Climate*, *23*(2), 282–293. https://doi.org/10.1175/2009jcli2978.1

Lau, K.-M., & Chan, P. (1986). Aspects of the 40–50 day oscillation during the northern summer as inferred from outgoing longwave radiation. *Monthly Weather Review*, *114*(7), 1354–1367. https://doi.org/10.1175/1520-0493(1986)114<1354:aotdod>2.0.co;2

Lavender, S. L., & Matthews, A. J. (2009). Response of the West African monsoon to the Madden–Julian oscillation. *Journal of Climate*, *22*(15), 4097–4116. https://doi.org/10.1175/2009jcli2773.1

Li, W., Zhu, Y., Zhou, X., Hou, D., Sinsky, E., Melhauser, C., et al. (2019). Evaluating the MJO prediction skill from different configurations of NCEP GEFS extended forecast. *Climate Dynamics*, *52*(7), 4923–4936. https://doi.org/10.1007/s00382-018-4423-9

Liebmann, B., Hendon, H. H., & Glick, J. D. (1994). The relationship between tropical cyclones of the western Pacific and Indian Oceans and the Madden-Julian oscillation. *J. Meteorol. Soc. of Japan*, *72*(3), 401–412. https://doi.org/10.2151/jmsj1965.72.3_401

Liebmann, B., & Smith, C. A. (1996). Description of a complete (interpolated) outgoing longwave radiation dataset [Dataset]. Bulletin of the American Meteorological Society, *77*(6), 1275–1277. Retrieved from https://www.jstor.org/stable/26233278

Lim, Y., Son, S.-W., & Kim, D. (2018). MJO prediction skill of the subseasonal-to-seasonal prediction models. *Journal of Climate*, *31*(10), 4075–4094. https://doi.org/10.1175/jcli-d-17-0545.1

Lin, H., Brunet, G., & Derome, J. (2008). Forecast skill of the Madden–Julian oscillation in two Canadian atmospheric models. *Monthly Weather Review*, *136*(11), 4130–4149. https://doi.org/10.1175/2008mwr2459.1

Madden, R. A., & Julian, P. R. (1971). Detection of a 40–50 day oscillation in the zonal wind in the tropical Pacific. *Journal of the Atmospheric Sciences*, *28*(5), 702–708. https://doi.org/10.1175/1520-0469(1971)028<0702:doadoi>2.0.co;2

Madden, R. A., & Julian, P. R. (1972). Description of global-scale circulation cells in the tropics with a 40–50 day period. *Journal of the Atmospheric Sciences*, *29*(6), 1109–1123. https://doi.org/10.1175/1520-0469(1972)029<1109:dogscc>2.0.co;2

Maloney, E. D., & Hartmann, D. L. (2000a). Modulation of eastern North Pacific hurricanes by the Madden–Julian oscillation. *Journal of Climate*, *13*(9), 1451–1460. https://doi.org/10.1175/1520-0442(2000)013<1451:moenph>2.0.co;2

Maloney, E. D., & Hartmann, D. L. (2000b). Modulation of hurricane activity in the Gulf of Mexico by the Madden-Julian oscillation. *Science*, *287*(5460), 2002–2004. https://doi.org/10.1126/science.287.5460.2002

Mason, S. J., & Graham, N. E. (1999). Conditional probabilities, relative operating characteristics, and relative operating levels. *Weather and Forecasting*, *14*(5), 713–725. https://doi.org/10.1175/1520-0434(1999)014<0713:cproca>2.0.co;2

Moore, R. W., Martius, O., & Spengler, T. (2010). The modulation of the subtropical and extratropical atmosphere in the Pacific basin in response to the Madden–Julian oscillation. *Monthly Weather Review*, *138*(7), 2761–2779. https://doi.org/10.1175/2010mwr3194.1

Mori, M., & Watanabe, M. (2008). The growth and triggering mechanisms of the PNA: A MJO-PNA coherence. *Journal of Meteorological Society of Japan*, *86*(1), 213–236. https://doi.org/10.2151/jmsj.86.213

Murphy, A. H., & Winkler, R. L. (1977). Reliability of subjective probability forecasts of precipitation and temperature. *Journal of the Royal Statistical Society*, *26*(1), 41–47. https://doi.org/10.2307/2346866

Nasuno, T. (2013). Forecast skill of Madden-Julian Oscillation events in a global nonhydrostatic model during the CINDY2011/DYNAMO observation period. *SOLA*, *9*(0), 69–73. https://doi.org/10.2151/sola.2013-016

Neena, J., Lee, J. Y., Waliser, D., Wang, B., & Jiang, X. (2014). Predictability of the Madden–Julian oscillation in the intraseasonal variability hindcast experiment (ISVHE). *Journal of Climate*, *27*(12), 4531–4543. https://doi.org/10.1175/jcli-d-13-00624.1

Pollard, R. T., Rhines, P. B., & Thompson, R. O. (1973). The deepening of the wind-mixed layer. *Geophysical Fluid Dynamics*, *4*(4), 381–404. https://doi.org/10.1080/03091927208236105

Putman, W. M., & Lin, S.-J. (2007). Finite-volume transport on various cubed-sphere grids. *Journal of Computational Physics*, *227*(1), 55–78. https://doi.org/10.1016/j.jcp.2007.07.022

Rashid, H. A., Hendon, H. H., Wheeler, M. C., & Alves, O. (2011). Prediction of the Madden–Julian oscillation with the POAMA dynamical prediction system. *Climate Dynamics*, *36*(3), 649–661. https://doi.org/10.1007/s00382-010-0754-x

Savarin, A., & Chen, S. S. (2022). Pathways to better prediction of the MJO–Part I: Effects of model resolution and moist physics on atmospheric boundary layer and precipitation. *Journal of Advances in Modeling Earth Systems*, e2021MS002928. https://doi.org/10.1029/2021MS002928

Seo, K.-H., & Lee, H.-J. (2017). Mechanisms for a PNA-like teleconnection pattern in response to the MJO. *Journal of the Atmospheric Sciences*, *74*(6), 1767–1781. https://doi.org/10.1175/jas-d-16-0343.1

Stan, C., Straus, D. M., Frederiksen, J. S., Lin, H., Maloney, E. D., & Schumacher, C. (2017). Review of tropical-extratropical teleconnections on intraseasonal time scales. *Review of Geophysics*, *55*(4), 902–937. https://doi.org/10.1002/2016rg000538

Swets, J. A. (1973). The relative operating characteristic in Psychology: A technique for isolating effects of response bias finds wide use in the study of perception and cognition. *Science*, *182*(4116), 990–1000. https://doi.org/10.1126/science.182.4116.990

Toth, Z., Talagrand, O., Candille, G., Zhu, Y., Jolliffe, I. T., & Stephenson, D. B. (2003). Probability and ensemble. Forecast verification: A Practitioner's guide in atmospheric science. Wiley.

Tseng, K.-C., Maloney, E., & Barnes, E. (2019). The consistency of MJO teleconnection patterns: An explanation using linear Rossby wave theory. *Journal of Climate*, *32*(2), 531–548. https://doi.org/10.1175/jcli-d-18-0211.1

Ventrice, M. J., Thorncroft, C. D., & Roundy, P. E. (2011). The Madden–Julian oscillation's influence on African easterly waves and downstream tropical cyclogenesis. *Monthly Weather Review*, *139*(9), 2704–2722. https://doi.org/10.1175/mwr-d-10-05028.1

Vitart, F. (2014). Evolution of ECMWF sub-seasonal forecast skill scores. *Quarterly Journal of the Royal Meteorological Society*, *140*(683), 1889–1899. https://doi.org/10.1002/qj.2256

Vitart, F., Ardilouze, C., Bonet, A., Brookshaw, A., Chen, M., Codorean, C., et al. (2017). The subseasonal to seasonal (S2S) prediction project database. *Bulletin of the American Meteorological Society*, *98*(1), 163–173. https://doi.org/10.1175/bams-d-16-0017.1

Wang, W., Hung, M.-P., Weaver, S. J., Kumar, A., & Fu, X. (2014). MJO prediction in the NCEP climate forecast system version 2. *Climate Dynamics*, *42*(9), 2509–2520. https://doi.org/10.1007/s00382-013-1806-9

Wheeler, M. C., & Hendon, H. H. (2004). An all-season real-time multivariate MJO index: Development of an index for monitoring and prediction. *Monthly Weather Review*, *132*(8), 1917–1932. https://doi.org/10.1175/1520-0493(2004)132<1917:aarmmi>2.0.co;2

Wheeler, M. C., Hendon, H. H., Cleland, S., Meinke, H., & Donald, A. (2009). Impacts of the Madden–Julian oscillation on Australian rainfall and circulation. *Journal of Climate*, *22*(6), 1482–1498. https://doi.org/10.1175/2008jcli2595.1

Wu, J., Ren, H.-L., Zuo, J., Zhao, C., Chen, L., & Li, Q. (2016). MJO prediction skill, predictability, and teleconnection impacts in the Beijing climate center atmospheric general circulation model. *Dynamics of Atmospheres and Oceans*, *75*, 78–90. https://doi.org/10.1016/j.dynatmoce.2016.06.001

Zhang, C. (2005). Madden-Julian oscillation. *Review of Geophysics*, *43*(2). https://doi.org/10.1029/2004rg000158

Zhang, C. (2013). Madden–Julian oscillation: Bridging weather and climate. *Bulletin of the American Meteorological Society*, *94*(12), 1849–1870. https://doi.org/10.1175/bams-d-12-00026.1

Zhou, L., Lin, S.-J., Chen, J.-H., Harris, L. M., Chen, X., & Rees, S. L. (2019). Toward convective-scale prediction within the next generation global prediction system. *Bulletin of the American Meteorological Society*, *100*(7), 1225–1243. https://doi.org/10.1175/bams-d-17-0246.1